

Performance Characteristics of Micro Crystal Element (MiCE) Detectors

Robert S. Miyaoka, *Member, IEEE*, Steve G. Kohlmyer, and Tom K. Lewellen, *Member, IEEE*

Abstract—Two micro crystal element (MiCE) detector unit designs are evaluated. The detector units are built using highly packed arrays of $0.8 \times 0.8 \times 6$ mm mixed lutetium silicate (MLS) crystals. The first detector unit, MiCE1, consists of a 5×5 array of $0.8 \text{ mm} \times 0.8 \text{ mm} \times 6 \text{ mm}$ MLS crystals. The detector unit is coupled to four channels of a Hamamatsu multichannel photomultiplier tube (PMT) via a 2×2 array of $2 \text{ mm} \times 2 \text{ mm}$ square optical fibers. The crystal of interaction is determined using simple Anger style logic. Light is shared within the crystal array to help facilitate decoding of the crystals. A full detector module will consist of a 4×4 array of detector units coupled to a 64-channel PMT. The second detector unit, MiCE2, consists of an array of $0.8 \text{ mm} \times 0.8 \text{ mm} \times 6 \text{ mm}$ MLS crystals directly coupled to a $6 + 6$ cross-anode PMT. The crystal of interaction is determined using simple Anger style logic. In both designs, individual crystals are well visualized. Simulations were performed to determine the imaging characteristics of a detector system consisting of MiCE1 detector modules (12.8-cm ring diameter). Results indicate that a detector system built with our MiCE detectors will have an image resolution of less than 1 mm for the central 2 cm of the field of view.

Index Terms—High-resolution positron emission tomography (PET) detectors, small animal PET.

I. INTRODUCTION

THE need for <1 mm image resolution for positron emission tomography (PET) is being driven by research in genetics (where the mouse is the main laboratory animal). Physically, spatial resolution is limited by positron range, noncollinearity of the photons, and the size of the resolution element of the detector system. However, the image resolution of the highest resolution scintillator-based PET system [1] is still limited by the size of the crystals (versus positron range or noncollinearity). In this paper, we investigate the decoding characteristics of detector modules built with $0.8 \times 0.8 \text{ mm}^2$ cross-section lutetium oxyorthosilicate (LSO) crystals [2]. We call our detectors the micro crystal element (MiCE) detectors.

II. MATERIALS AND METHODS

A. MiCE1

The MiCE1 detector unit was built with $0.8 \times 0.8 \times 6 \text{ mm}^3$ mixed lutetium silicate (MLS) crystals.¹ The physical properties

Manuscript received November 3, 2000; revised June 11, 2001. This work was supported in part by PHS under Grant CA86892.

R. S. Miyaoka and T. K. Lewellen are with the Radiology Department, University of Washington, Seattle, WA 98195 USA (e-mail: rmiyaoka@u.washington.edu; tkldog@u.washington.edu).

S. G. Kohlmyer is with General Electric Medical Systems, Waukesha, WI 98195 USA (e-mail: steve.kohlmyer@med.ge.com).

Publisher Item Identifier S 0018-9499(01)08649-X.

¹Unified Technologies Advanced Research International, Richmond, BC, Canada.

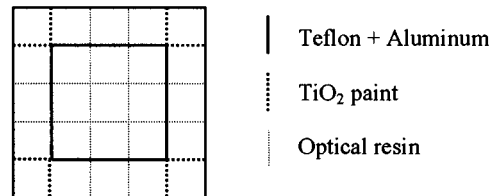


Fig. 1. Crystal interfaces for MiCE1 detector unit.



Fig. 2. Picture of sample MiCE1 detector unit resting on a dime.

of MLS are very similar to LSO and are listed together in Table I. Five sides of the crystals were polished; one $0.8 \times 0.8 \text{ mm}^2$ side was left unpolished and faced away from the PMT. Each detector unit consists of a 5×5 crystal array connected to a 64-channel PMT² via a 2×2 array of $2 \times 2 \text{ mm}^2$ cross-section optical fibers. The optical fibers were ~ 6 cm long. The crystal of interaction is determined using simple ratio logic [3]. Light is shared within the crystal array to help facilitate decoding of the crystals. The design of the crystal-crystal interfaces for the detector unit is illustrated in Fig. 1. Optical resin is used to allow light sharing along an interface. TFE Teflon, aluminum foil, and TiO_2 paint are used as opaque reflectors. The inner 3×3 array of crystals was first wrapped with a single layer of TFE Teflon for optimum light collection efficiency. The aluminum foil was used to make the interface opaque while minimizing the spacing between neighboring crystals. TiO_2 paint was used because it facilitated the construction of the detector unit. A full detector module will consist of a 4×4 array of optically isolated detector units coupled to a 64-channel PMT. A sample detector unit is illustrated in Fig. 2.

Crystal maps and energy spectra were produced using signals from either four or 12 channels of the PMT, as shown in Fig. 3. Only four channels were directly coupled to each detector unit. Signals from the neighboring channels were due to light sharing within the entrance window of the PMT. Data were collected with the detector unit coupled to the PMT at two locations: 1) the central four channels of the PMT and 2) a set of four channels at the corner of the PMT. When the detector unit was coupled to

²Hamamatsu, R5900-00-M64.

TABLE I
SCINTILLATOR CHARACTERISTICS

	BGO	LSO	MLS
Density (g/cm ³)	7.13	7.4	7.30-7.39
Effective Atomic Number	74	66	63-65
Linear Atten. Coeff. (cm ⁻¹)	0.96	0.87	~0.85
Decay Constant	300	40	36-39
Light Output (% NaI(Tl))	15	60	65-75

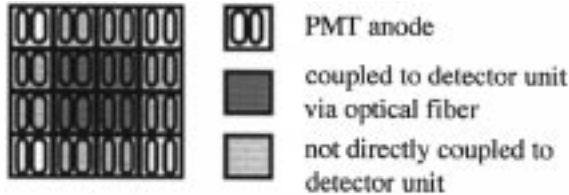


Fig. 3. Sixteen channels of 64-channel PMT. Detector unit is directly coupled to central four channels via optical fibers. Event is positioned using either four or 12 signals.

the corner of the PMT, only the four channels directly coupled to the detector unit were used to generate the crystal maps.

Crystal maps were made using simple ratio logic. Gain balancing between channels was done in software and values were initially based upon channel gain values provided by the factory. Gains for the four channels directly coupled to the detector unit were further adjusted to align the photopeaks of the corner four crystals. Crystal maps were generated from singles data (i.e., not coincidence data) using a ⁶⁸Ge point source. A program was written to determine the individual crystal boundaries within the crystal map. By binning the data in *X*, *Y*, and energy, the energy spectra for each individual crystal could be acquired. The data used to look at the energy spectra characteristics of the detector unit were collected in coincidence using a ⁶⁸Ge point source.

B. MiCE2

The MiCE2 detector was built with the same $0.8 \times 0.8 \times 6$ mm³ MLS crystals. Our goal is to decode a 25×25 array of crystals using a 12 (6+ 6)-channel cross-plate anode PMT.³ The advantages of using the R5900-00-C12 PMT versus the R5900-00-M64 are threefold.

- 1) The PMTs are less expensive.
- 2) For the same outer package size, the minimum effective area of the photocathode is larger (i.e., 22 versus 18 mm).
- 3) Because of the larger effective photocathode area, it may be feasible to couple the MLS crystals directly to the PMT and still have a minimal gap between detector modules when placed in a ring configuration.

Methods to tightly pack crystal arrays while still keeping the crystals optically isolated were investigated. We are using a grid, illustrated in Fig. 4, made of a highly reflective multilayer polymer material [4] to house the crystals. The grid illustrated can be used to construct a 24×24 crystal detector module. The mirror film was slotted, as illustrated in the figure, using an ultraviolet laser (i.e., solid-state tripled YAG laser with a wavelength of 355 nm). Properties of the mirror film material are listed in Table II. The grids were hand-assembled and took ~90

³Hamamatsu, R5900-00-C12.

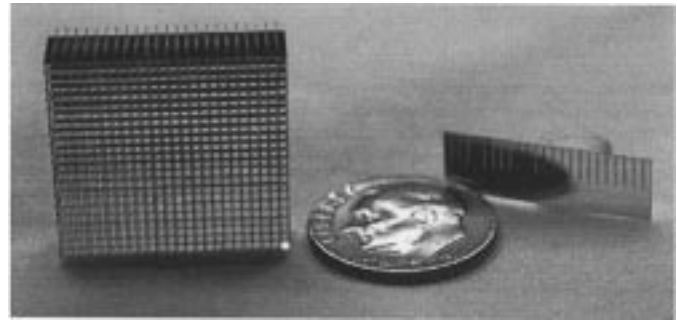


Fig. 4. Illustration of MiCE2 detector grid. Grid is made of a multilayer polymer mirror material that has been laser cut as shown in the illustration (right side of picture).

TABLE II
CHARACTERISTICS OF MULTILAYER POLYMER MIRROR FILM

Luminous Reflectivity (LR)	>98%
Bandwidth (>90% LR)	(400-415)-(775-1020) nm
Transmits Wavelengths	>775-1020 nm
Absorbs Wavelengths	<400 nm
Usage Angle	0-90 degrees
Thickness	2.4-2.7 mils

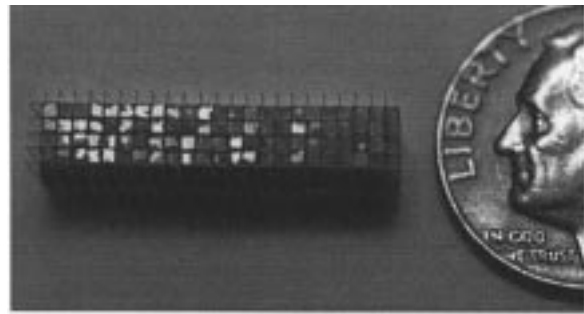


Fig. 5. Illustration of 22×4 MLS crystal MiCE2 detector. Detector unit is shown next to a dime.

min to build. Once the grid was assembled, the MLS crystals were slid into the openings.

A 22×4 crystal detector module was assembled, illustrated in Fig. 5. Each of the crystals was polished on five sides. The side facing away from the PMT was left unpolished. The size of the detector array was limited by the number of crystals we currently possess with the proper surface treatment. Once assembled, the detector array was directly coupled to a R5900-00-C12 PMT using BC-630 optical coupling grease.⁴ The individual signals from the PMT were fed to a resistor network that produces four position signals (*X*+, *X*-, *Y*+, *Y*-). Crystal maps were produced using simple Anger style logic. Only singles data were collected (i.e., not coincidence data) using a ⁶⁸Ge point source.

C. Simulation Studies

Detector system simulations were performed using the SimSET software package [5]. Extensions to the current release were added to allow full Monte Carlo tracking of photon interactions in the detector modules [6]. Events were positioned according to the weighted average of interactions

⁴Bicron, Newbury, OH.

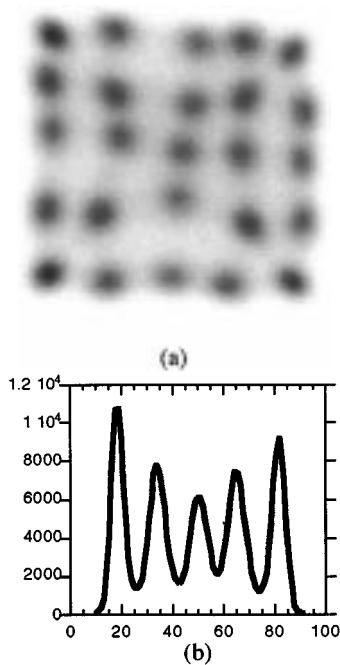


Fig. 6. (a) Crystal map using 12 PMT channels with gain adjustment. (inverse grayscale) (b) Profile of counts in lower row of crystal map.

in the detector block. The effects of positron range and photon noncollinearity were included in the simulations. The option to model coherent scatter was set to off.

The detector system consisted of 24 detector modules and had an inner ring diameter of 12.8 cm. The detector system was simulated as having 22% energy resolution and a 250–650 keV energy window. The data were binned into 256 by 400 distance-angle sinograms. Each distance bin was 0.2 mm. A pseudowobble was incorporated in the detector binning procedure to support the sinogram binning requirements [6]. Simulations were performed to determine the image resolution at different radial positions (0.1, 1.0, and 2.0 cm off-center) in the field of view (FOV). The two-dimensional direct and cross-slice data, containing the point source, were reconstructed using filtered back projection with a 0.4-mm ramp filter. The radial and tangential components of the reconstructed point sources were measured.

III. RESULTS AND DISCUSSION

A. MiCE1

A crystal map for the MiCE1 detector unit is shown in Fig. 6(a). The map illustrated was formed using the 12-channel data with the detector unit coupled to the central four channels of the PMT. All 25 crystals are easily visualized using four or 12 channels of data. The profile of the bottom row of crystals is displayed in Fig. 6(b). The average peak-to-valley ratio for the row of crystals is 5.3. The average peak-to-valley ratio for the same row of crystals using the four-channel data to generate the crystal map is 4.4 (not shown).

The composite energy spectrum for the full detector unit is shown in Fig. 7. A sample energy spectrum for a specific crystal is illustrated in Fig. 8. The energy resolution for the crystal

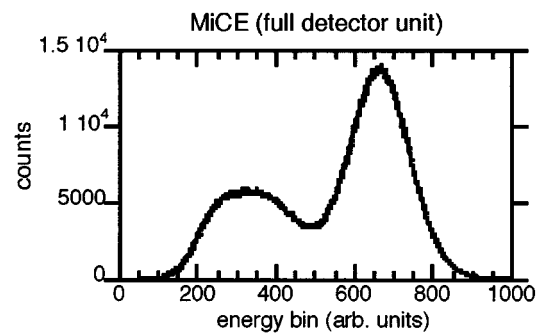


Fig. 7. Composite energy spectrum for the MiCE1 detector unit.

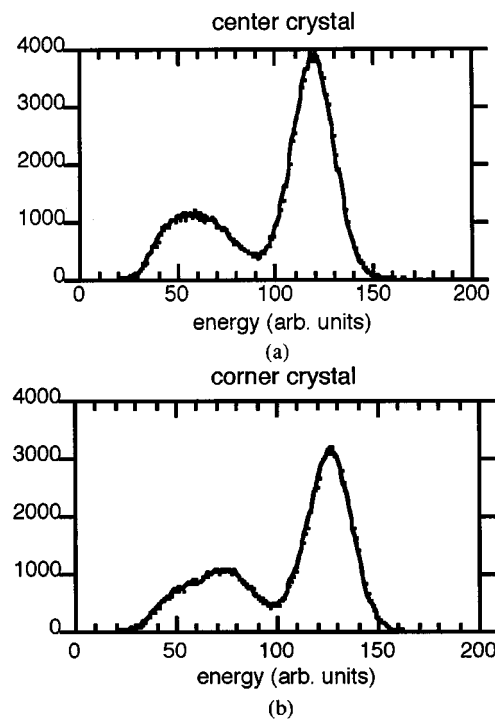


Fig. 8. Energy spectra for individual MiCE1 detector unit crystals: (a) the center crystal and (b) a corner crystal.

shown is 20%. The range of energy resolutions for the crystals in the block is 20–27%, with most being around 21%.

The crystal map for the MiCE1 detector unit coupled to the corner of the PMT is illustrated in Fig. 9. Again, all 25 crystals are easily visualized. The average peak-to-valley ratio for the bottom row of crystals is 4.8. The composite energy spectrum for the detector unit is illustrated in Fig. 10. The range of energy resolutions for the individual crystals in the detector unit is 17 to 27%, with most crystals having an energy resolution of $\sim 21\%$.

B. MiCE2

A crystal map for the 22×4 MiCE2 detector array, with the long axis of the array along the x -axis of the PMT, is illustrated in Fig. 11. All 88 crystals are easily visualized. A profile through the lower row of crystals is illustrated in Fig. 12. The average peak-to-valley ratio for the row of crystals is 4.1. All crystals were also easily visualized with the detector array positioned along the y -axis (results not shown). The average peak-to-valley ratio for a column of crystals along the y -axis is 4.7.

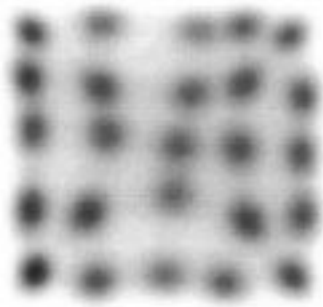


Fig. 9. Crystal map for MiCE1 detector unit coupled to corner channels of PMT. Average peak-to-valley ratio of lower row of crystals is 4.8 (inverse grayscale).

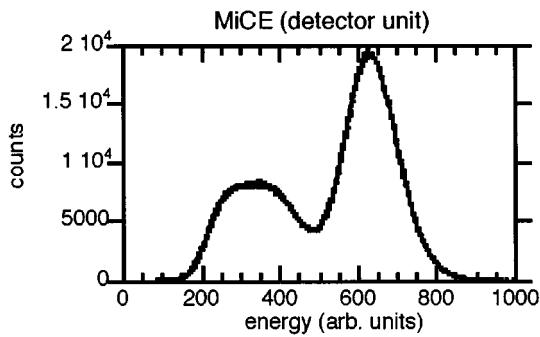


Fig. 10. Composite energy spectrum for MiCE1 detector unit coupled to corner channels of PMT.

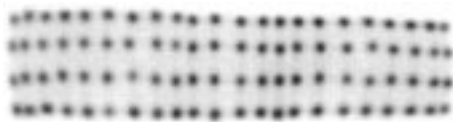


Fig. 11. Crystal map for 22×4 array of crystals (MiCE2 design). All crystals are easily visualized (inverse grayscale).

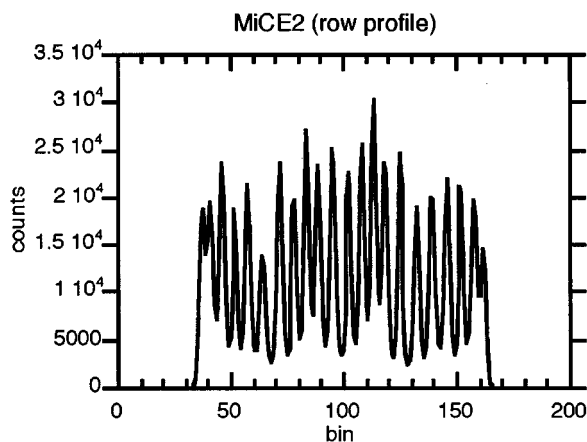


Fig. 12. Profile of counts in lower row of crystal map (i.e., in dotted box). Average peak-to-valley ratio of profile is 4.1.

The composite energy spectrum for all 88 crystals is shown in Fig. 13. The photopeak of the energy spectrum is broadened because of differences in the light collection efficiency between crystals at the center and the edge of the PMT. Overall, the energy resolution for individual crystals is $\sim 16\%$. Energy spectra from two crystals are illustrated in Fig. 14. The crystals were

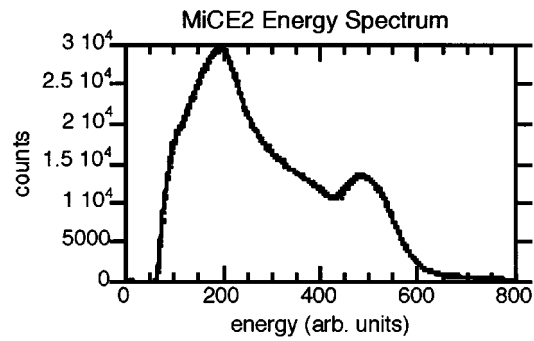


Fig. 13. Composite energy spectrum for MiCE2 detector unit.

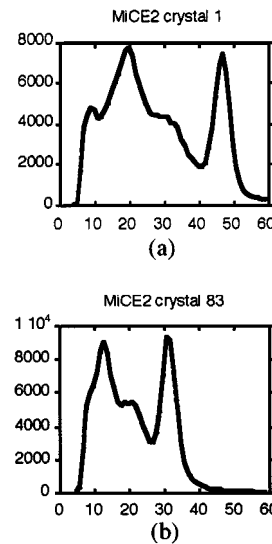


Fig. 14. Sample energy spectra from individual crystals. Notice shift in photopeak positions between the two crystals: crystal located (a) in central region of detector array and (b) at edge of crystal array.

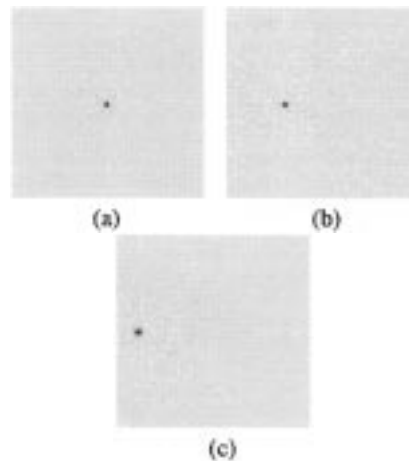


Fig. 15. Images of reconstructed point source offset by (a) 0.1, (b) 1.0, and (c) 2.0 cm (inverse grayscale).

selected to illustrate the significant difference in light collection efficiency for crystals positioned near the center of the detector array and crystals positioned near the edge of the window of the PMT.

Similar results were collected with the detector array positioned along the y -axis (results not shown).

C. Simulation Studies

Images of the reconstructed point source are illustrated in Fig. 15. The radial and tangential image resolutions for a point source at 0.1, 1.0, and 2.0 cm from the center of the FOV are 0.8, 0.9, and 1.2 mm (radial) and 0.9, 0.9, and 0.9 mm (tangential), respectively.

The characteristic broadening of the radial response function for sources away from the center of the FOV is evident even when using 6-mm crystals. The effect should be small when imaging mice, where most of the structures of interest will be within ± 1 cm of the center of the FOV; however, it will begin to become noticeable if the system is used to image larger animals.

IV. CONCLUSION

Both MiCE designs work well and should be able to decode arrays using even smaller cross-section crystals. The average energy resolution for the MiCE1 detector unit was $\sim 21\%$. The average energy resolution for the MiCE2 detector unit was not determined; however, the energy resolution for many of the crystals looked at was better than the MiCE1 design. Because light collection efficiency was not a problem for either module, we are considering going to slightly longer crystals (e.g., 8 or 10 mm) to increase the detection sensitivity of our system. We are

also planning to extend our MiCE2 design to work with the new flat-panel PMTs when they become available.

ACKNOWLEDGMENT

The authors thank J. Grierson, Ph.D., for bringing the multi-layer polymer film material to their attention. They also thank UTAR International for providing them with samples of MLS crystals during the MiCE1 phase of this work.

REFERENCES

- [1] A. Chatziioannou and S. R. Cherry *et al.*, "Performance evaluation of microPET: A high-resolution lutetium oxyorthosilicate PET scanner for animal imaging," *J Nucl. Med.*, vol. 40, no. 7, pp. 1164–75, 1999.
- [2] C. L. Melcher and J. S. Schweitzer, "Cerium-doped lutetium oxyorthosilicate: A fast, efficient new scintillator," *IEEE Trans Nucl. Sci.*, vol. 39, pp. 502–5, Aug. 1992.
- [3] M. E. Casey and R. Nutt, "A multislice two dimensional BGO detector system for positron emission tomography," *IEEE Trans Nucl. Sci.*, vol. NS-33, pp. 460–3, 1986.
- [4] M. F. Weber, C. A. Stover, L. R. Gilbert, T. J. Nevitt, and A. J. Ouder Kirk, "Giant birefringent optics in multilayer polymer mirrors," in *Science*, vol. 287, Mar. 31, 2000, pp. 2451–6.
- [5] R. L. Harrison *et al.*, "Preliminary experience with the photon history generator module of a public-domain simulation system for emission tomography," in *Conf. Rec. IEEE Nucl. Sci. Symp.*, 1993, pp. 1154–8.
- [6] R. S. Miyaoka and T. K. Lewellen, "Effect of detector scatter on the decoding accuracy of a DOI detector module," *IEEE Trans Nucl. Sci.*, vol. 47, no. 4, pp. 1614–19, Aug. 2000.